Brain Medical Image Fusion Using $L2$-Norm-Based Features and Fuzzy-Weighted Measurements in 2-D Littlewood–Paley EWT Domain

Xin Jin, Qian Jiang, Xing Chu, Xun Lang, Shaowen Yao, Keqin Li, *Fellow, IEEE*, and Wei Zhou, *Member, IEEE*

Abstract— Computational imaging provides comprehensive and reliable information about human tissue for medical diagnosis and treatment, with medical image fusion as one of the most important technologies in the field. Empirical mode decomposition (EMD), a promising model for image processing, has been used for image fusion in some methods. However, the varying number of decomposed layers leads to problems using EMD for image fusion. In this article, we propose a fusion method for medical images incorporating $L2$-norm-based features, a match/salience/fuzzy-weighted measure, and the 2-D Littlewood–Paley empirical wavelet transform (2-D LPEWT) as new version of EMD. We first decompose medical images with LPEWT to obtain the residual component (residue) and detailed sub-images that are named as intrinsic mode functions (IMFs). Then we extract the regional features of residue with an $L2$-norm-based model to fuse the residue while simultaneously fusing IMFs using a method combining a fuzzy membership function with a match/salience measurement. Finally, we reconstruct the comprehensive image by applying inverse LPEWT to the fused residue and IMFs. We evaluated our method using a frequently-used data set of brain images. The results show that our proposed method is more effective than conventional methods by fusing more information into the final images. We also show a feasible scheme for applying EMD to image fusion.

Index Terms— Biomedical imaging, empirical Littlewood–Paley empirical wavelet transform (LPEWT), empirical mode decomposition (EMD), fuzzy set theory, image fusion, $L2$-norm.

I. INTRODUCTION

A. Motivation

MEDICAL imaging technology offers tremendous advantages for clinical medicine by providing accurate information about body tissues and structures [1]. Medical images of the brain combining data from different sensors show complementary details reflecting the imaging mechanisms of the different sensors [2]–[4]. Medical images incorporating different brain image models provide physicians with reliable and abundant physiological information, which is meaningful for clinical diagnosis, radiotherapy planning, and so on [5]–[7].

Magnetic resonance imaging (MRI) and computerized tomography (CT) are the most popular technologies in medical diagnosis and treatment, resulting in the fusion of these technologies becoming a hotbed of research activity [5], [7]. CT images primarily show high-density tissue details, while MRI images clearly show features of tissue with higher moisture content [2], [5], [6]. Conventional medical image fusion methods fall roughly into three categories: spatial-domain methods, transform-domain methods, and hybrid methods.

Classical spatial domain includes neural network [8], [9], independent component analysis (ICA) [11], principal component analysis (PCA) [12], and fuzzy sets [13]. Spatial-domain methods normally produce a decision or weight map for fusing the source medical images [14]. The advantages of these methods are the simplicity and ease of implementation and their lower computational costs. However, spatial-domain methods are unable to represent edges and outlines completely and lose many detailed image features in the fusion process. Recently, deep learning is also used for image fusion that can be regarded as spatial-domain-based fusion method [9]. A neural network model is first trained by a large-scale image data set to represent significant features that can be used for image fusion. However, it is difficult to collect and build a large enough medical image data set for fusion model training. Transform-domain methods are popular in medical image fusion and include pyramid transform (PT) [15], discrete wavelet transform (DWT) [16], contourlet transform [17], shearlet transform (ST) [18], tetrolet transform [19], and sparse representation (SR) [10]. Transform-domain methods first transform the medical images into a specific domain to obtain subimages that are then fused by one or more fusion rules before producing a final image via an inverse transform. However, most transform-domain methods have limitations as well. Some, such as the Laplacian pyramid, fail to describe the outline and contrast of images accurately. Others, including DWT, contourlet transform, and ST, fail to capture salient features effectively, causing artifacts and Gibbs effects in the fused images. SR is an innovative image processing technique

that relies on a learned over-complete dictionary to represent image features, and fusion rule is then used for coefficient selection. However, there are still some limitations for SR, such as computational complexity and information loss [10].

To overcome the lack of the shift-invariance property of the conventional transform-domain-based methods, others have proposed the nonsubsampled contourlet transform (NSCT) [20] and nonsubsampled ST (NSST) [21] to restrain the pseudo-Gibbs phenomena around singularities [22], [23]. However, these nonsubsampled methods have heavy computational requirements from the large number of subimages having the same size as the source images [24].

Hybrid methods combine the spatial and transform domains, which means that the fusion rule of transform-domain image fusion method is on the basis of the fusion rule of spatial-domain method generally. Specifically, hybrid methods fuse the transformed subimages using spatial-domain methods, such as the combination of NSST and neural networks [23], Laplacian pyramid decomposition and neural networks [25], and PCA and shift-invariant wavelet transforms [26].

After it was proposed, the empirical mode decomposition (EMD) method was also introduced into image fusion as the same as preceding conventional transform methods, including medical image fusion [27]–[30]. EMD can decompose source image into a residue to present the approximate representation and a set of intrinsic mode functions (IMFs) to describe the details of the image. The performance of EMD-based medical image fusion is affected by the capacity of the empirical decomposition model, which exerts a significant influence on overall image fusion performance [28]. Also, researchers have proposed many promising EMD models with excellent possibilities for improving the performance of EMD-based medical image fusion. Gilles [39] and Gilles *et al.* [41] represented a series of empirical wavelet (wavelet-like) decomposition methods similar to EMD. One of them, empirical wavelet transform (EWT), was promptly used for automated glaucoma diagnosis [31], hyperspectral image classification [32], and fault diagnosis [33]. As a result, we consider EWT to have enormous potential for medical image fusion. Multiple source images have unequal numbers of IMFs, which is the first problem to be solved in order to introduce EWT into medical image fusion. The second problem is the challenge of feature extraction and fusion rules.

B. Our contributions

Motivated by the preceding analysis, we propose fusing multimodal medical images from MRI and CT brain images into a synthetic result. We do this by first decomposing source images into a set of subimages (residue and IMFs) and defining an operation to solve the different numbers of decomposed subimages from different source images using Littlewood–Paley EWT (LPEWT). Second, we design $L2$-norm-based features to fuse the residue components. Third, we use a match/salience/fuzzy-weighted measure (MSFM) to fuse the IMF components. Finally, we reconstruct the fused image according to the fused subimages. Our work has three main contributions.

1) We introduce 2-D Littlewood–Paley empirical wavelet transform (2-D LPEWT) into medical image fusion because of the competitive performance and clear theoretical background and define an operation to solve the changeable numbers of the IMFs of different source images. We show a feasible and effective scheme to apply EMD to image fusion.
2) We design an $L2$-norm-based feature extraction method to fuse the residue based on $L2$-norm theory because the main features of the residue can be described effectively, and the method is a new regional feature representation method to show detailed information in medical images.
3) We introduce a modified match/salience measure using a fuzzy membership function (MF) to fuse IMFs according to the distribution of IMF coefficients. In this method, we combine the match/salience measure with fuzzy set theory, which represents the regional and amplitude features of the IMF coefficient simultaneously.

We show that LPEWT can be used for medical image fusion, even with differing numbers of decomposed layers. We also use two regional feature-based fusion strategies. Our experimental results reveal that our proposed method is more effective than conventional methods in extracting and fusing tissue information into final images.

The remainder of this article is organized as follows. Section II discusses the principles of 2-D LPEWT. Section III describes our proposed brain medical image fusion scheme in detail. Section IV presents our experimental results and subsequent discussion. Section IV concludes this article.

II. 2-D LPEWT

Huang *et al.* [34] designed a method called EMD to extract amplitude modulated-frequency modulated components of a 1-D signal. This method differed from conventional transform methods such as wavelet transforms [35]. EMD first detects the upper and lower envelopes to represent the global trend of the input signal and then subtracts the envelopes from the signal to obtain the remaining component, and then repeats these processes until it obtains a set of IMFs components (high frequency) and a residue component (low frequency) [36], [39]. Nunes *et al.* [37] introduced a bidimensional version of EMD for image analysis, and then Tian *et al.* [38] proposed an image fusion method also using an EMD approach. However, classical EMD's problem is its lack of theoretical background for detecting envelopes.

Gilles [39] constructed a new EMD-like model called EWT that used the wavelet to extract the amplitude modulated-frequency modulated components of an input image (signal) by designing a suitable wavelet filter bank. EWT first detects the Fourier supports to build the corresponding wavelet filters and then uses the resulting filter bank to filter the input image to separate the components. Afterward, the method constructs the LPEWT from its namesake theory [40], [41], which determines supports in the Fourier domain according to the analyzed image. Gilles *et al.* [41] proposed LPEWT, employing an empirical approach to detect the inner and outer

radius of each annuli support (centered around the origin) in the Fourier domain. This enables separation of the image's Fourier energy according to the supports and, correspondingly, the image's information as well. The advantage of this procedure is that it considers the Fourier plane in a polar representation. The remainder of the section regularly refers to the theory and calculation methods of 2-D LPEWT.

2-D LPEWT first calculates the pseudo-polar FFT [42], [43] denoting it as the operator $F_p(f)(\theta, |\omega|)$

$$F_p(f)(\omega_1, \omega_2) = \sum_{x_1=0}^{N-1} \sum_{x_2=0}^{N-1} f(x_1, x_2) \exp(-i(x_1\omega_1 + x_2\omega_2)) \tag{1}$$

where $f(x)$ is the 2-D signal in the spatial domain, N is the size of an input image pixels, $x = (x_1, x_2)$ is a spatial position in the 2-D plane, and $\omega = (\omega_1, \omega_2)$ denotes the coordinates in the 2-D frequency plane.

For each angle, the corresponding average spectrum is computed as

$$\tilde{F}(|\omega|) = \frac{1}{N_\theta} \sum_{i=0}^{N_\theta - 1} F_p(f)(\theta_i, |\omega|) \tag{2}$$

where N_θ is the number of discrete angles.

Gilles *et al.* [41] introduced a modified Fourier boundaries detection method based on their previous work in [39]. First, the method detects all local maxima M_i of H (a signal in Fourier domain) and deduces the corresponding position ω_i. It then keeps the set of all ω_i corresponding to the $n - 1$ largest maxima and re-indexes them as ω_n, where $1 \leq n \leq N - 1$. Finally, it deduces the set of Fourier boundaries $\Omega = \omega^n{}_{n=0,...,n}$ using $\omega^0 = 0; \omega^N = \pi; \omega^n = 0.5(\omega_n + \omega_{n-1})$. Of note, these values are in the interval $[0, \pi]$ and $\omega^0 = 0$ and $\omega^N = \pi$ by convention. Thus, we can get

$$\omega^0 = 0; \quad \omega^N = \pi; \quad \omega^n = 0.5(\omega_n + \omega_{n-1}) \text{ for } 1 \leq n \leq N - 1.$$

However, this method only considers local information (i.e., spectrum magnitude) and disregards the spectrum global trend. To overcome this problem, a simple way was proposed to preserve the position of the lowest minima in the segment defined by consecutive maxima. A set of all local minima located between ω_{n-1} and ω_n was denoted as $\mho_n$, then

$$\omega^0 = 0, \quad \omega^N = \pi, \quad \omega^n = \mathrm{argmin}(\mho_n) \text{ for } 1 \leq n \leq N - 1.$$

Even so, many local maxima still belong to a common mode and may induce many unexpected boundaries. To avoid this problem, the logarithm of is calculated to remove the global trend, which is denoted $T(\omega)$ in the analyzed spectrum prior to detection. In this article, we use the "plaw" option [41]. We approximate H to a power law of the form $T(\omega)^{-s}$ and estimate the exponent S using a least-mean square criterion. In its discrete version, this is equivalent to

$$s = \mathrm{argmin}||H(\omega) - \omega^{-s}||_2 = -\frac{\sum_n \ln \omega_n \ln H(\omega_n)}{\sum_n \ln (\omega_n)^2}.$$

Finally, the automatic algorithm [44] detects the modes that represent a histogram of the energy distributed by frequency. From this, we are able to detect the Fourier boundaries.

2-D LPEWT performs the modified Fourier boundaries detection on $\hat{F}(|\omega|)$ to obtain the set of spectral radius, denoted by $\{\omega^n\}_{n=0,1...,N}$ (with $\omega^0 = 0$ and $\omega^N = \pi$), that is used to build the set of 2-D empirical Littlewood–Paley wavelets $B^{\varepsilon L\rho} = \{\phi_1(x), \{\psi_n(x)\}_{n=1}^{N-1}\}$

$$F_2(\phi_1)(\omega) = \begin{cases} 1, & \text{if } |\omega| \leq (1-\gamma)\omega^1 \\ \cos\left[\frac{\pi}{2}\beta\left(\frac{1}{2\gamma\omega^1}(|\omega| - (1-\gamma)\omega^1)\right)\right] \\ & \text{if } (1-\gamma)\omega^1 \leq |\omega| \leq (1+\gamma)\omega^1 \\ 0, & \text{otherwise.} \end{cases}$$

If $n \neq N - 1$, then

$$F_2(\psi_n)(\omega) = \begin{cases} 1, & \text{if } (1+\gamma)\omega^n \leq |\omega| \leq (1-\gamma)\omega^{n+1} \\ \cos\left[\frac{\pi}{2}\beta\left(\frac{1}{2\gamma\omega^{n+1}}(|\omega| - (1-\gamma)\omega^{n+1})\right)\right] \\ & \text{if } (1-\gamma)\omega^{n+1} \leq |\omega| \leq (1+\gamma)\omega^{n+1} \\ \sin\left[\frac{\pi}{2}\beta\left(\frac{1}{2\gamma\omega^n}(|\omega| - (1-\gamma)\omega^n)\right)\right] \\ & \text{if } (1-\gamma)\omega^n \leq |\omega| \leq (1+\gamma)\omega^n \\ 0, & \text{otherwise.} \end{cases}$$

If $n = N - 1$, then

$$F_2(\psi_{N-1})(\omega) = \begin{cases} 1, & \text{if } (1+\gamma)\omega^{N-1} \leq |\omega| \\ \sin\left[\frac{\pi}{2}\beta\left(\frac{1}{2\gamma\omega^{N-1}}(|\omega| - (1-\gamma)\omega^{N-1})\right)\right] \\ & \text{if } (1-\gamma)\omega^{N-1} \leq |\omega| \leq (1+\gamma)\omega^{N-1} \\ 0, & \text{otherwise.} \end{cases}$$

In the equations of $F_2 = (\phi_1)(\omega)$, $F_2 = (\psi_n)(\omega)$, and $F_2 = (\psi_{N-1})(\omega)$, β is an arbitrary $C^k|[0, 1]|$ function, fulfilling the properties $\beta(x) = 0$ if $x \leq 0$, $\beta(x) = 1$ if $x \geq 1$, and $\beta(x) + \beta(1 - x) = 1$, $\forall x \in [0, 1]$; γ ensures that two consecutive transition areas do not overlap. Furthermore, there is an additional necessary condition on γ as given in [34]. Then the 2-D empirical Littlewood–Paley transform of an input image f is given by

$$W_f^{\varepsilon L\rho}(n, X) = F_2^*(F_2(f)(\omega)\overline{F_2(\psi_n)(\omega)})$$

with the detail and approximation coefficients (conventionally denoted as $W^{\eta L\rho}(0, x)$) given by

$$W_f^{\varepsilon L\rho}(0, X) = F_2^*(F_2(f)(\omega)\overline{F_2(\phi_1)(\omega)})$$

where F_2 and F_2^* are the usual 2-D Fourier transform and its inverse.

At last, the empirical Littlewood–Paley wavelets $B^{\varepsilon L\rho}$ and the 2-D LPEWT coefficients $W^{\varepsilon L\rho}(n, x)$ are output.

We obtain the inverse transform is obtained by the adjoint formulation

$$f(x) = F_2^*\big(F_2\big(W_f^{\varepsilon L\rho}\big)(0, \omega)F_2(\phi_1)(\omega) \\ + \sum_{n=1}^{N-1} F_2\big(W_f^{\varepsilon L\rho}\big)(n, \omega)F_2(\psi_n)(\omega)\big)).$$

Other works provide detailed information concerning the processes and theoretical basis of 2-D LPEWT [39]–[44].
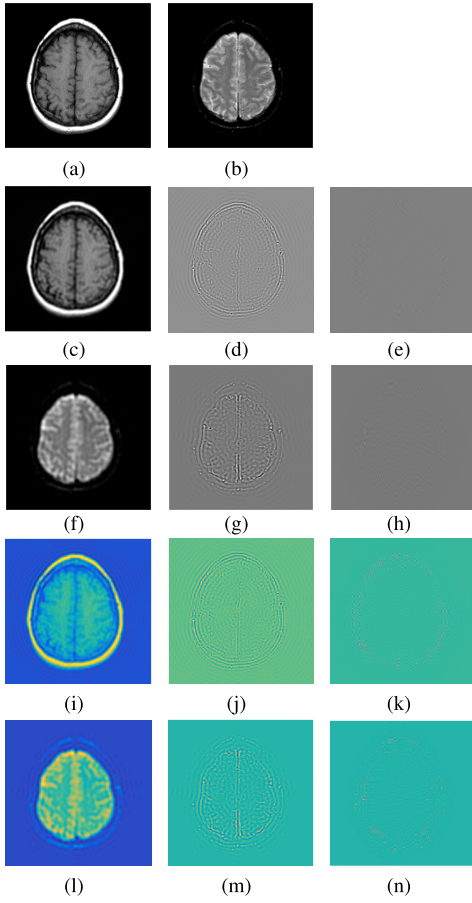
Fig. 1. First example of 2-D LPEWT. (a) CT_A. (b) MRI_B. (c) R_ A. (d) IMF_ A 1. (e) IMF_ A 2. (f) R_ B. (g) IMF_ B 1. (h) IMF_ B 2. (i) Pseudo-color image of CT_A. (j) Pseudo-color image of IMF_ A 1. (k) Pseudo-color image of IMF_ A 2. (l) Pseudo-color image of R_ B. (m) Pseudo-color image of IMF_B 1. (n) Pseudo-color image of IMF_ B 2.
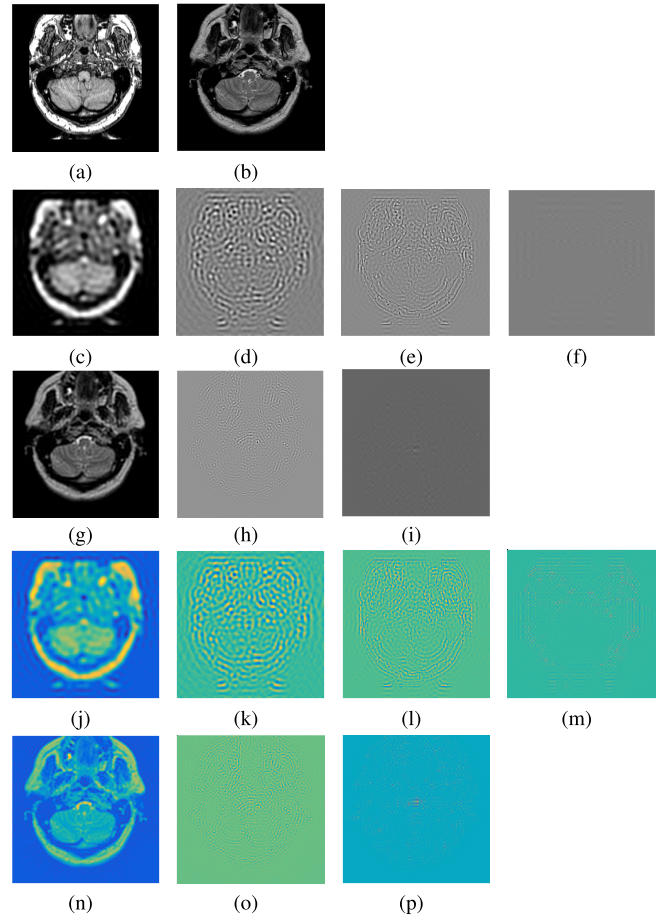

Fig. 2. Second example of 2-D LPEWT. (a) CT_C. (b) MRI_D. (c) R_C. (d) IMF_C 1. (e) IMF_C 2. (f) IMF_C 3. (g) R_D. (h) IMF_ D1. (i) IMF_ D 2. (j) Pseudo-color image of R_C. (k) Pseudo-color image of IMF_C 1. (l) Pseudo-color image of IMF_C 2. (m) Pseudo-color image of IMF_C 3. (n) Pseudo-color image of R_D. (o) Pseudo-color image of IMF_D1. (p) Pseudo-color image of IMF_D 2.

Figs. 1 and 2 show the examples of CT and MRI brain images processed with 2-D LPEWT. In Fig. 1, the numbers of subimages (residue and IMFs) from the two source images are equal as is common with conventional transform methods. However, the number of IMF subimages in Fig. 2 is different, showing that the fusion processes should be specially designed when compared with the fusion rulers of other conventional transform methods. The subimages and their pseudocolor images in the 2-D LPEWT domain show that the main features of the brain images are readily visible, demonstrating the possibility of fusing them into a comprehensive image effectively.

III. PROPOSED SCHEME

In this article, we propose a brain medical image fusion method incorporating 2-D LPEWT, *L*2-norm-based features, and fuzzy set theory. The fusion scheme consists of four steps: 2-D LPEWT decomposition, residual fusion, IMFs fusion, and 2-D LPEWT reconstruction. We make three broad contributions. First, we introduce a new version of EWT, named 2-D LPEWT, for medical image decomposition. Second, we demonstrate fusion of residuals using *L*2-norm-based features. Third, we synthesize IMFs using a measure

incorporating MSFM. The following five Sections detail each of these aspects.

A. *L*2-Norm-Based Features

The norm, associated with the concept of length, often measures the length or size of each vector in a vector space (or matrix). The vector space for such a norm is called a normed vector space [45]–[47]. Specifically, the norm is the sum of the positive lengths (sizes) of all vectors in a vector space or matrix, which means that the larger the matrix (the vector), the larger the norm.

In image fusion, the detailed features of a brain image, which are the critical factors determining the quality of the fused image, are represented by the pixel amplitude (coefficient) and the regional information from the adjacent pixels (coefficients). The specific region or area within an image can be regarded as a vector space (matrix), and the value of pixel or coefficient can be regarded as a vector of the vector space. Thus, we find the features of medical image can be addressed by norm theory that provides the physical

fundamental the feature extraction of brain image, which is useful for representing detailed features of brain images.

For an n-dimensional space $x = (x_1, x_2, \ldots, x_n)$, we obtain the ρ-norm denoted as $L\rho$-norm with

$$\|x\|_\rho = \sqrt[\rho]{\sum_{i=1}^{n} |x_i|^\rho}$$

where $P \geq 1$ is an integer. For example, there is the $L1$-norm ($\rho = 1$) and the $L2$-norm ($\rho = 2$).

$L2$-norm is popular norm, and it is often used in many engineering and science disciplines [45], [48], [49]. The $L2$-norm is defined as

$$\|x\|_2 = \sqrt[2]{\sum_{i=1}^{n} |x_i|^2}.$$

We can further rewrite it as

$$\|x\|_2 = \sqrt[2]{\sum_{i=1}^{n} x_i^2}.$$

For image, we can get the $L2$-norm-based features as

$$\mathrm{LN}(i, j) = \sqrt[2]{\sum_{i=1}^{M} \sum_{j=1}^{N} \mathrm{im}(i, j)^2}$$

where LN denotes the $L2$-norm-based features of an image, M and N are the size of an image, and $\mathrm{im}(i, j)$ is a pixel value at row i and column j in the image.

The $L2$-norm is often used as a standard quantity for measuring the vector difference of a vector space.

Inspired by the $L2$-norm and regional features of an image, the $L2$-norm-based feature represents the detailed information in brain images. We first calculate the $L2$-norm for rows of an image and then the columns. The equations are as follows:

$$\mathrm{LN}_R(i, j) = \sqrt{\sum_{i=1}^{p} \sum_{j=2}^{p} \mathrm{im}(i, j)^2 + \mathrm{im}(i, j-1)^2}$$

and

$$\mathrm{LN}_C(i, j) = \sqrt{\sum_{i=2}^{p} \sum_{j=1}^{p} \mathrm{im}(i, j)^2 + \mathrm{im}(i-1, j)^2}$$

where p is the window size, and $\mathrm{im}(i, j)$ is a pixel value at row i and column j in the image; LN_R and LN_C denote the rows and columns $L2$-norm-based features of an image, respectively.

We then calculate the $L2$-norm-based features as

$$\mathrm{LN}(i, j) = \frac{1}{p^2}(\mathrm{LN}_R(i, j) + \mathrm{LN}_C(i, j))$$

where p is the window size, and $\mathrm{im}(i, j)$ is a pixel value at row i and column j in the image.

Fig. 3 depicts two samples of $L2$-norm-based features and their pseudocolor images and clearly shows brain image features including the regional distribution and intensity of
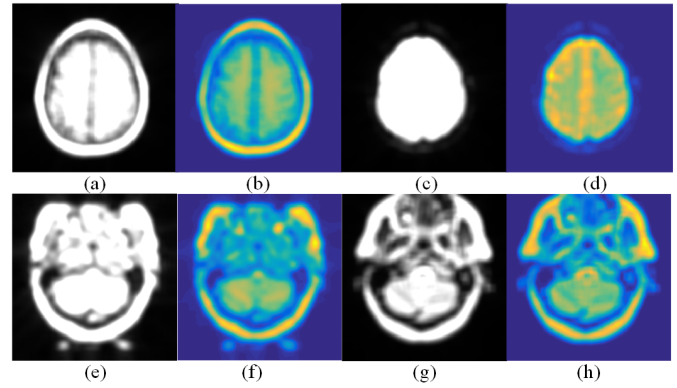

Fig. 3. Two examples of $L2$-norm-based features. (a) $L2$-norm-based features of R_A. (b) Pseudo-color image of $L2$-norm-based features from R_A. (c) $L2$-norm-based features from R_B. (d) Pseudo-color image of $L2$-norm-based features from R_B. (e) $L2$-norm-based features from R_C. (f) Pseudo-color image of $L2$-norm-based features from R_C. (g) $L2$-norm-based features from R_D. (h) Pseudo-color image of $L2$-norm-based features from R_D.

features (the hot areas and cool areas in the pseudo-color image). Thus, our proposed $L2$-norm-based feature extraction method provides the necessary information for medical image fusion.

B. Residue Fusion

In the context of 2-D LPEWT, residue describes an approximate representation of an image, such as the statistical distribution of pixel values or the coarse, large-scale structure of the tissue. This information is very important for medical image fusion. As shown in Figs. 1 and 2, the large-scale features of the brain image are represented in the residues, so the residue fusion method exerts a big influence on the fusion effect. As shown in Fig. 3, the $L2$-norm-based features describe the structure of the brain images with the amplitude, which makes it easy to determine the residue coefficient of different brain images.

According to the amplitude of the $L2$-norm-based features, we define the fusion rule as

$$\mathrm{Residue}_F (i, j) = \begin{cases} \mathrm{Residue}_A (i, j), & \mathrm{LN}_A (i, j) \geq \mathrm{LN}_B (i, j) \\ \mathrm{Residue}_B (i, j), & \mathrm{LN}_A (i, j) < \mathrm{LN}_B (i, j) \end{cases} \quad (3)$$

where $\mathrm{Residue}_F$ is the fused residue, $\mathrm{Residue}_A$ and $\mathrm{Residue}_B$ are the residues from brain images A and B, and LN_A and LN_B are the $L2$-norm-based features from brain images A and B.

Fig. 4 shows that the key features of the residues of two image pairs are effectively integrated into the fused images when compared with the original residues, as with the coarse edges and structural features.

C. IMFs Fusion

The IMFs of 2-D LPEWT, which contain the high-frequency components, represent the detailed features of the brain image in small scale, including textures and sharp edges. Among transform domain-based image fusion methods, maximum
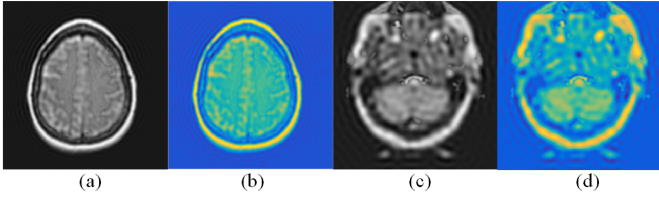
Fig. 4. Fused residues of the first and second examples. (a) Fused residues of the first example. (b) Pseudo-color image of the first example. (c) Fused residues of the second example. (d) Pseudo-color image of the second example.
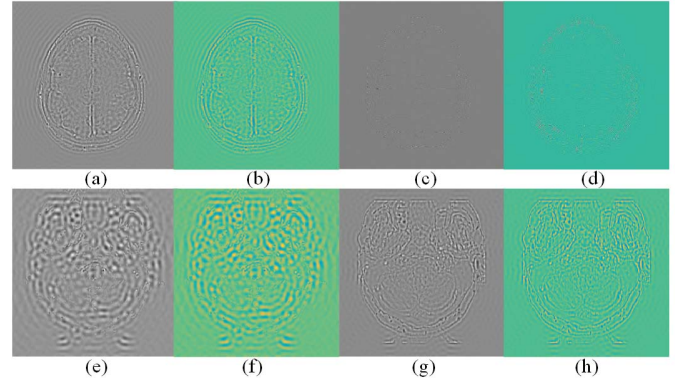

Fig. 5. Fused IMF of the first and second examples. (a) Fused IMF_F 1 for the first example. (b) Pseudo-color image of the fused IMF_F 1 for the first example. (c) Fused IMF_F 2 for the first example. (d) Pseudo-color image of the fused IMF_F 2 for the first example. (e) Fused IMF_F 1 for the second example. (f) Pseudo-color image of the fused IMF_F 1 for the second example. (g) IMF_F 2 for the second example. (h) Pseudo-color image of the fused IMF_F 2 for the second example.

selection [29], [50] is one of the most popular for the fusion of the decomposed subimages because the amplitude of the subimage coefficient (pixel) can represent the change of intensity of the detailed feature in high-frequency sub-images. Maximum selection's shortcoming is that the fusion decision only considers a single coefficient and ignores the regional information important for medical diagnosis. There-fore, a region-aware method should be used in the medical image fusion task. It is obvious that both the regional infor-mation and the amplitude of the IMFs coefficient make needed contributions to brain image fusion, so we propose a modified salience/match measure based on the research of Burt and Kolczynski [51] and use it for the IMFs fusion within 2-D LPEWT, calling it the MSFM because of its inclusion of match and salience measures along with a fuzzy-weighted calculation.

The salience measure, which is widely used in fusing infrared and visible images, demonstrates the importance of an IMF coefficient in the 2-D LPEWT domain. Generally, the important coefficient of IMF is tend to more salience than the unimportant one. We use Burt's calculation of the salience measure [51]

$$S(i, j) = 2 \sum_{m=1}^{w} \sum_{n=1}^{h} P(m, n) S_0(i - m, j - n)$$

where $S(i, j)$ is the salience measure of IMF, and $S_0(i, j) = \text{IMF}(i, j)\text{IMF}(i, j)$; $\text{IMF}(i, j)$ is the IMF coefficient; P is the local window for extracting the regional features.

The match measure not only represents the amplitude information of the corresponding coefficient in IMFs but also describes the regional features of two IMFs. We define M_{AB} of IMFs of two source images

$$M_{AB}(i, j) = \frac{2 \sum_{m=1}^{w} \sum_{n=1}^{h} P(m, n) M_0(i - m, j - n)}{S_A(i, j) + S_B(i, j) + \varepsilon}$$

where $M_0(i, j) = \text{IMF}_A(i, j)\text{IMF}_B(i, j)$, $\text{IMF}_A(i, j)$ is the IMF coefficient from source image A, $\text{IMF}_B(i, j)$ is the IMF coefficient from source image B, P is the local window for extracting the regional features of IMF, $S_A(i, j)$ is the salience measure of IMF A, $S_B(i, j)$ is the salience measure of IMF B, and ε is a small number to avoid the denominator becoming 0.

Having introduced the match/salience measure, we now define some symbols relating to the fuzzy set theory-based

IMF fusion processes. ind_1 is a flag indicating whether the match measure of IMF A and IMF B is high or low, and ind_2 is a flag indicating if the salience of IMF A and IMF B is the highest or lowest. W_A and W_B are the weightings of IMF A and IMF B, with $W_A + W_B = 1$. Therefore, our fusion strategy has two situations.

First, if the match measure between IMFs is high (i.e., $M_{AB}(i, j) > \alpha$ and $\text{ind}_1(i, j) = 1$, for a given value of α, which we set at 0.75), then the coefficient from the IMFs with the highest salience is weighted as the final coefficient (that is, $S_A(i, j) > S_B(i, j)$, so $\text{ind}_2(i, j) = 1$). In this case, we define the fusion rule

$$\text{IMF}_F(i, j) = W_A(i, j)\text{IMF}_A(i, j) + W_B(i, j)\text{IMF}_B(i, j)$$

where W_A and W_B are the weighted values of IMF A and IMF B with the computation of the weights as explained in the next paragraph.

Fuzzy set theory has been widely used in image fusion in recent years, achieving competitive performance in many fields. The MF of fuzzy set theory quantifies the affiliation relationship of an element (coefficient) belonging to a given set (clear area or fuzzy area). The value of the MF is in the interval [0, 1], with 0 meaning full non-membership and 1 meaning full membership. Values between 0 and 1 indicate degrees of affiliation. We use the fuzzy MF to determine the weightings of IMF_A and IMF_B. According to the distribution of the values of M_{AB}, we use a Gaussian MF (GMF) to construct a new weighted method instead of a linear function and ensure our restrictions according to the following equations.

1) $W_{\max} > W_{\min}$.
2) $W_{\min} = 0.5 - e^{-\frac{(M_{AB} - c)^2}{2\sigma^2}}$.
3) $W_{\max} = 1 - W_{\min} = 0.5 + e^{-\frac{(M_{AB} - c)^2}{2\sigma^2}}$

where the standard deviation σ of M_{AB} is calculated as

$$\sigma = \sqrt{\frac{1}{w \times h} \sum_{i=1}^{w} \sum_{j=1}^{h} (M_{AB} - c)^2}$$
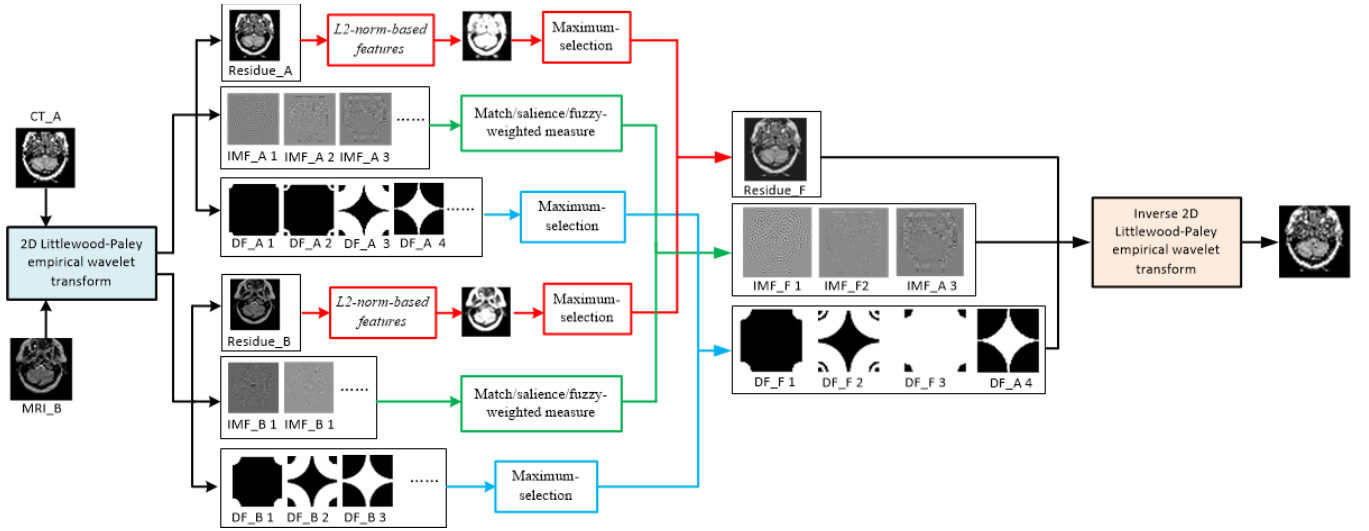
Fig. 6.   Diagram of the proposed brain medical image fusion method.

and the mean value c of M_{AB} is calculated as

$$c = \frac{1}{w \times h} \sum_{i=1}^{w} \sum_{j=1}^{h} M_{AB}$$

where M_{AB} is the match measure, and w and h define the size of M_{AB}. The larger weight $W_{\max}$ is assigned to the IMF with the larger salience. If $S_A(i, j) > S_B(i, j)$, $W_A = W_{\max}$ and $W_A = W_{\min}$, otherwise $W_A = W_{\min}$ and $W_B = W_{\max}$.

As a result, we can rewrite the fusion rule as

$$F_1 = \text{ind}_1 \left(\begin{matrix} \text{ind}_2 W_{\max} \text{IMF}_A + \text{ind}_2 W_{\min} \text{IMF}_B \\ + \cdots (1 - \text{ind}_2) W_{\min} \text{IMF}_A \\ + (1 - \text{ind}_2) W_{\max} \text{IMF}_B \end{matrix} \right). \quad (4)$$

Second, if the match measure is low (i.e., $\text{ind}_1(i, j) = 0$), then coefficients for both IMFs are fused according to ind_1 and ind_2. If $M_{AB}(i, j) \leq \alpha$, then $W_{\max} = 1$ and $W_{\min} = 0$. In this case, we define the fusion rule

$$F_2 = (1 - \text{ind}_1)(\text{ind}_2 \text{IMF}_A + (1 - \text{ind}_2)\text{IMF}_B).$$

Finally, we merge the fusion rules of the two situations according to the IMFs of the two brain images:

$$\begin{aligned} F &= F_1 + F_2 \\ &= \text{ind}_1(\text{ind}_2 W_{\max} \text{IMF}_A + \text{ind}_2 W_{\min} \text{IMF}_B \\ &\quad + \cdots (1 - \text{ind}_2) W_{\min} \text{IMF}_A + (1 - \text{ind}_2) W_{\max} \text{IMF}_B) \\ &\quad + \cdots (1 - \text{ind}_1)(\text{ind}_2 \text{IMF}_A + (1 - \text{ind}_2)\text{IMF}_B). \end{aligned}$$

Fig. 5 shows the fused IMFs from the first and second examples, showing that detailed features of the brain images are effectively extracted as compared with the subimages in Figs. 1 and 2.

D. Detected Filters Integration

In 2-D LPEWT, we obtain an appropriate set of detection filters (DFs) according to the different brain images. Each DF can be regarded as a decision map because most of values in the filters are 0 or 1. The DFs are useful for

describing the features during brain image reconstruction, and the number of DFs is the same as the number of corresponding brain subimages (residue and IMFs) [41]. Thus, we adopt a simple but effective method of the maximum selection to integrate the DFs for the fused brain image reconstruction

$$\text{DF}_F(i, j) = \begin{cases} \text{DF}_F(i, j), & \text{DF}_F(i, j) \geq \text{DF}_B(i, j) \\ \text{DF}_B(i, j), & \text{DF}_F(i, j) < \text{DF}_B(i, j) \end{cases}$$

where DM_F is the set of integrated filters, DF_A is the set of DFs of brain image A, and DF_B is the set of DFs of brain image B.

E. Fusion Strategies and Steps

The varying number of IMFs of different source images in EMD is a common problem requiring special treatment. In 2-D LPEWT, the discrepant IMFs often represent the fine features of brain images. Specifically, a CT image may have one more IMFs than an MRI image. Because the fine features of the extra IMFs of an image are not available in the nonexistent counterpart image, we preserve these features completely in the fused image. Thus, we implement a check to see which image has more IMFs. We assign the "extras" from the image with more IMFs to the fused IMF at the beginning. Regular fusion processes then handle the remaining IMF pairs to obtain the fused IMFs as the substitution of initial IMFs correspondingly; thus the extra IMFs can be kept, and the IMF pairs are fused correspondingly.

Fig. 6 depicts the diagram of our proposed brain medical image fusion method. The detailed steps are represented in Algorithm 1 Processes (Strategies and Steps).

IV. EXPERIMENTS AND ANALYSIS

We performed experiments with our method to validate our approach by using medical images from the Whole Brain Atlas at Harvard Medical School (http://www.med.harvard.edu/aanlib/home.html), and the basic elements in these images are regarded as pixels that represent

Algorithm 1 Processes (Strategies and Steps)

Step 0: Input source images A and B.

Step 1: Decompose the source image A and B with 2D LPEWT to obtain residue A (R_A) and residue B (R_B), IMF_A and IMF_B, detection filters A (DF_A) and detection filters B (DF_B).

Step 2: Extract the L2-norm-based features to fuse the residue of source images A and B:
  R_F = Residue_fusion (R_A, R_B)

Step 3: Address the situation where the images have different numbers of IMFs:
  [mA] = number(IMF_A)
  [mB] = number(IMF_B)
  If (mA>mB)
    IMF_F(1:mA) = IMF_A(1: mA)
    DF_F(1:mA) = DF_A(1: mA)
    m = mB
  else
    IMF_F(1: mB) = IMF_B(1: mB)
    DF_F(1: mB) = DF_B(1: mB)
    m = mA
  end

Step 4: Fuse the IMFs using the MFSM:
  For i = 1 to m
    IMF_F(i) = IMF_fusion (IMF_A(i), IMF_B(i))
  End

Step 5: Integrate the DFs using the maximum-selection method:
  For i = 1 to m
    DF_F(i) = maximum_selection(DF_A (i), DF_B(i))
  End

Step 7: Reconstruct the comprehensive image with the fused residue, IMFs, and the detection filters and inverse 2D LPEWT.
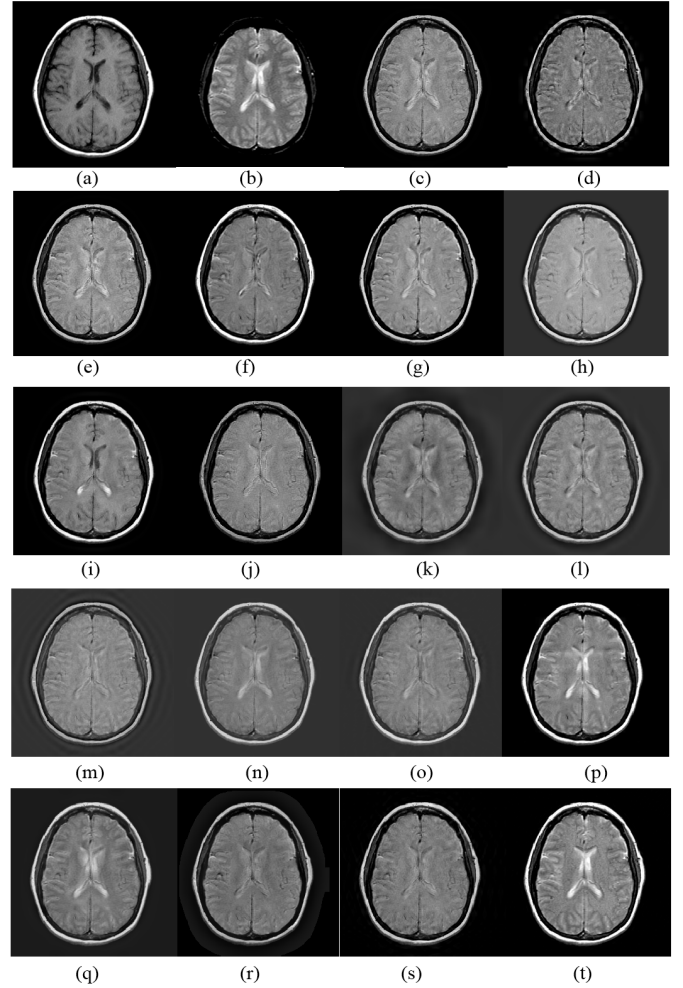

Fig. 7. Experiments for S1. (a) CT. (b) MRI. (c) GP [52]. (d) DWT [52], [53]. (e) fsdP [52]. (f) GFS [54]. (g) CSR [55]. (h) ASR [56]. (i) GFF [57]. (j) MSVD [58]. (k) DTDWT [59]. (l) SWT [60] [61]. (m) CVT [62]. (n) DTCWT-SR [63]. (o) CVT-SR [63]. (p) LRSDL [64]. (q) PCLLE [65]. (r) MSGIF [66]. (s) DCHWT [67]. (t) Proposed.

one 1-mm brain tissue. Moreover, the size of the image is 256 × 256 pixel (the gray-scale value from 1 to 256). Our method are compared with several common image fusion methods including gradient pyramid (GP) [52], DWT [52], [53], filter-subtract-decimate pyramid (fsdP) [52], guided image filter and image statistics (GFS) [54], convolutional SR (CSR) [55], adaptive SR (ASR) [56], guided filtering fusion (GFF) [57], multiresolution singular value decomposition (MSVD) [58], dual-tree complex DWT (DTDWT) [59], stationary wavelet transform (SWT) [60], [61], curvelet transform (CVT) [62], dual-tree complex wavelet transform-SR (DTCWT-SR) [63], CVT-SR [63], LRSDL [64], PCLLE [65], MSGIF [66], and DCHWT [67].

Besides, we used common objective evaluation metrics for different methods in our experiment: edge information preservation value (Q^{abf}) [68], total loss of information (L^{abf}) [68], mutual information (Q^{MI}) [69], Piellas metric (Q^{W}) [70], the phase congruency-based fusion metric (Q^{PC}) [71], nonlinear correlation information entropy (Q^{NCIE}) [72], quantitative evaluation-based on Tsallis entropy (Q^{te}) [73]. Q^{abf}

represents how much the edge feature is fused from the source images into the final image, the best value is 1, and the worst value is 0. L^{abf} is the total amount of information loss in image fusion processes; the best value is 0, and the worst value is 1. Q^{MI} measures the amount of information that is fused into the final image from the source images. Q^{W} can take the salience information into account to represent the quality of the final image. Q^{PC} compares the local cross correlation of corresponding feature maps between the source image and the final image. Q^{NCIE} is a nonlinear correlation metrics to represent the difference between the source image and final image. Q^{te} is a Tsallis entropy-based metric and can be regarded as a form of non-extensive entropy. For Q^{MI}, Q^{W}, Q^{PC}, Q^{NCIE}, and Q^{te}, the greater values are, the better the fused image is. All the adopted metrics are calculated according to both the source image and fused image. These methods can present the shared edge or information among source images and fused image. Thus, the information or features transformed from the source image to the fused image can be quantified.

TABLE I

AVERAGE INDEXES OF FUSED IMAGES GENERATED BY DIFFERENT METHODS (THE PARENTHESES REPRESENTS THE NUMBERS OF THE BEST METRIC IN THE EXPERIMENTS)

|	Q^{abf}	Q^{MI}	L^{abf}	Q^{te}	Q^{NCIE}	Q^{PC}	Q^{W}
GP [52]	0.5222	2.7233	0.4554	0.6063	0.8061	0.3774	0.7649
DWT [52] [53]	0.4947	2.4743	0.3676	0.5741	0.8055	0.2962	0.7667
fsdP [52]	0.5189	2.7066	0.4535	0.6020	0.8061	0.3632	0.7619
GFS [54]	0.6043	3.3454	0.3542	0.7887(2)	0.8083(2)	0.3706	0.8339
CSR [55]	0.5835	2.7896	0.4002	0.6753	0.8063	0.4565	0.7888
ASR [56]	0.5751	2.7778	0.4037	0.6762	0.8063	0.4596	0.7819
GFF [57]	0.6466	3.5915	0.3367	0.8185(1)	0.8100(1)	**0.5766**(5)	0.8342
MSVD [58]	0.4304	2.7073	0.5448	0.6523	0.8060	0.2902	0.7023
DTDWT [59]	0.5351	2.5983	0.3366	0.5875	0.8058	0.3486	0.8112
SWT [60] [61]	0.5296	2.5480	0.3484	0.5757	0.8057	0.3427	0.7996
CVT [62]	0.5034	2.5211	0.4067	0.5600	0.8056	0.3140	0.7670
DTCWT-SR [63]	0.5775	3.0629	0.3452	0.7125	0.8073	0.4137	0.8321
CVT-SR [63]	0.5189	2.7066	0.4535	0.6020	0.8061	0.3632	0.7619
LRSDL [64]	0.6393 (1)	3.4069	0.3089	0.7789	0.8086	0.4984 (1)	**0.8439** (6)
PCLLE [65]	0.6014	3.1893	0.3173	0.7228	0.8078	0.4563	0.8352
MSGIF [66]	0.4905	2.6070	0.3817	0.6530	0.8058	0.3092	0.7857
DCHWT [67]	0.5210	2.8058	0.4437	0.6077	0.8064	0.3509	0.8183
Proposed	**0.6556**(6)	**3.9071**(7)	**0.2487**(7)	**0.8664**(4)	**0.8111**(4)	0.5338(1)	0.8290 (1)
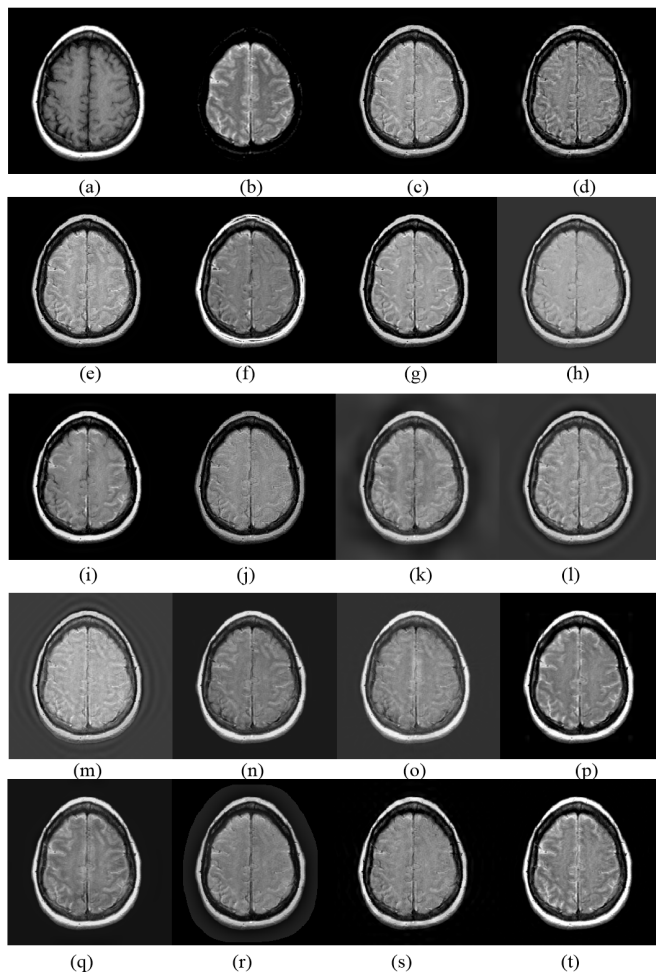
Fig. 8. Experiments for S2. (a) CT. (b) MRI. (c) GP [52]. (d) DWT [52], [53]. (e) fsdP [52]. (f) GFS [54]. (g) CSR [55]. (h) ASR [56]. (i) GFF [57]. (j) MSVD [58]. (k) DTDWT [59]. (l) SWT [60], [61]. (m) CVT [62]. (n) DTCWT-SR [63]. (o) CVT-SR [63]. (p) LRSDL [64]. (q) PCLLE [65]. (r) MSGIF [66]. (s) DCHWT [67]. (t) Proposed.
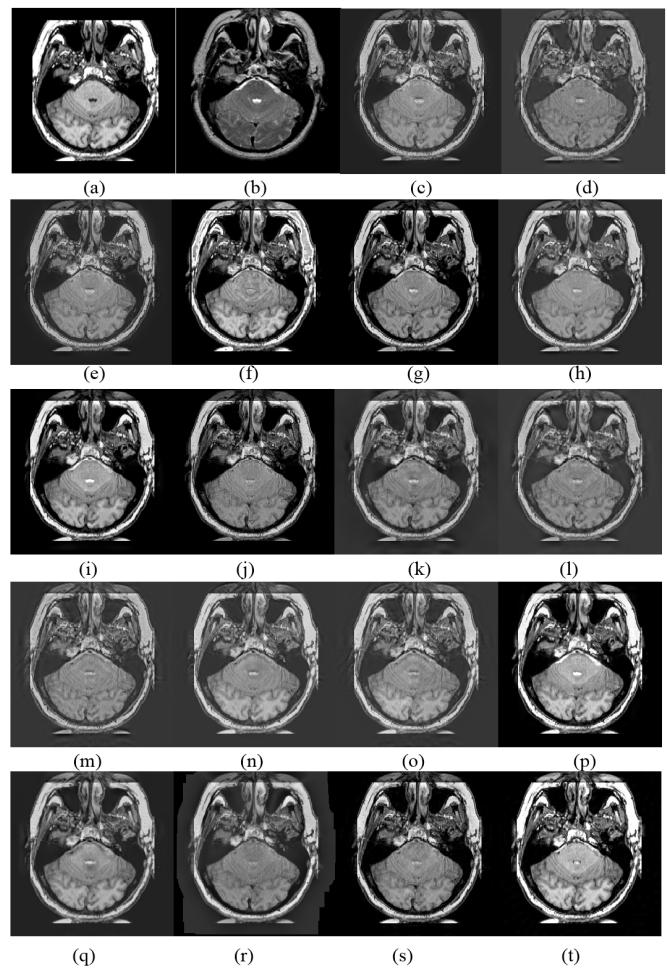

Fig. 9. Experiments for S3. (a) CT. (b) MRI. (c) GP [52]. (d) DWT [52], [53]. (e) fsdP [52]. (f) GFS [54]. (g) CSR [55]. (h) ASR [56]. (i) GFF [57]. (j) MSVD [58]. (k) DTDWT [59]. (l) SWT [60], [61]. (m) CVT [62]. (n) DTCWT-SR [63]. (o) CVT-SR [63]. (p) LRSDL [64]. (q) PCLLE [65]. (r) MSGIF [66]. (s) DCHWT [67]. (t) Proposed.

Fig. 7 shows the fused brain image from the first pair of source images. The brightness of the fused image generated by the proposed method is better than those of other methods.

The sharp edges of the skull were preserved, and the textures of the brain cell were fused into the final image. We judge the fused image generated by our proposed method to be better than those of the control methods.
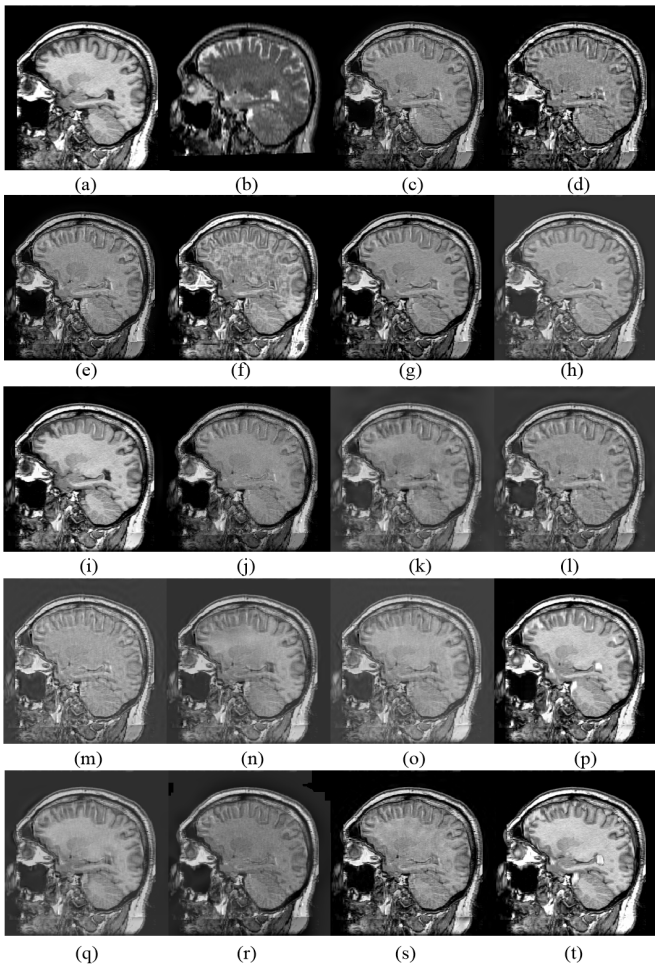
Fig. 10. Experiments for S4. (a) CT. (b) MRI. (c) GP [52]. (d) DWT [52], [53]. (e) fsdP [52]. (f) GFS [54]. (g) CSR [55]. (h) ASR [56]. (i) GFF [57]. (j) MSVD [58]. (k) DTDWT [59]. (l) SWT [60], [61]. (m) CVT [62]. (n) DTCWT-SR [63]. (o) CVT-SR [63]. (p) LRSDL [64]. (q) PCLLE [65]. (r) MSGIF [66]. (s) DCHWT [67]. (t) Proposed.
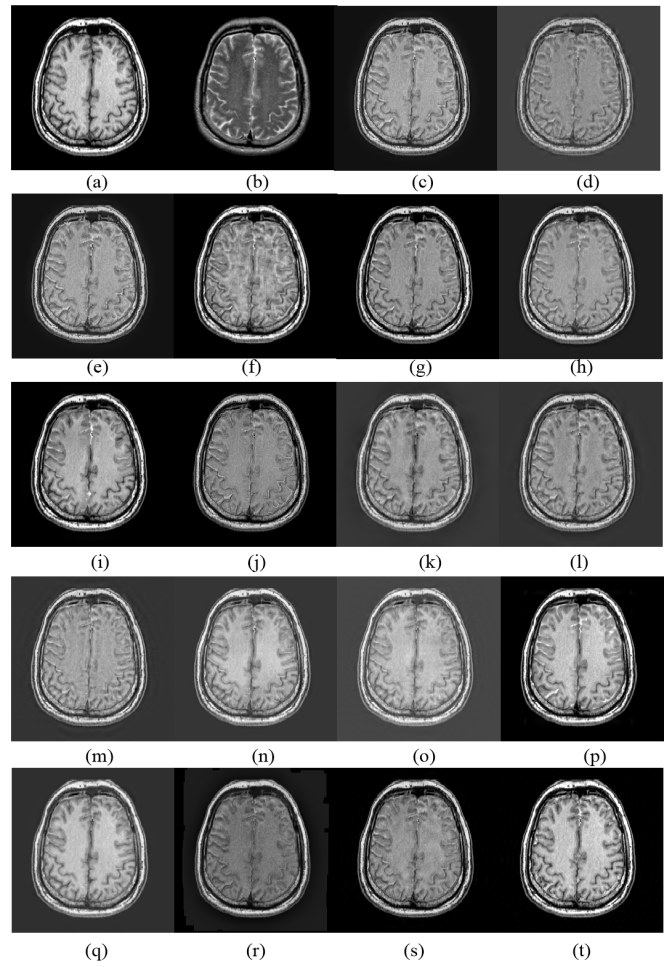

Fig. 11. Experiments for S5. (a) CT. (b) MRI. (c) GP [52]. (d) DWT [52], [53]. (e) fsdP [52]. (f) GFS [54]. (g) CSR [55]. (h) ASR [56]. (i) GFF [57]. (j) MSVD [58]. (k) DTDWT [59]. (l) SWT [60], [61]. (m) CVT [62]. (n) DTCWT-SR [63]. (o) CVT-SR [63]. (p) LRSDL [64]. (q) PCLLE [65]. (r) MSGIF [66]. (s) DCHWT [67]. (t) Proposed.

In Fig. 8, the bright edges of skull and brain were shown clearly in the fused image from our proposed method, and the textures and edges of the ectocinerea and alba were kept as well.

In Fig. 9, the contrast of the fused image from our proposed method is most similar to the source images than that of other methods. In addition, the human tissue information from the CT and MRI images is represented in the proposed method.

Fig. 10 shows the fused brain image for the fifth pair of source images. The fused images in Fig. 10(i) and (p) are better than those of other methods, especially with regard to contrast, brightness, and edge details. However, some important features were lost such as that relating to the moisture content of the MRI image. The fused image generated by our proposed method is better than that of the comparative methods.

In Fig. 11, the contrast and brightness of the fused image generated by our proposed method are better than those of other methods. Furthermore, our method introduced no unwelcome information. Fig. 11(f) shows some obvious artifacts in the areas of the ectocinerea and alba. The detailed feature and structural information of the brain medical images are well-preserved.

In Fig. 12, the main features of brain CT and MRI images are well integrated into the fused image generated by our proposed method, including the sharp edges of the skull and the textures of the brain, showing that our proposed method successfully extracted and fused the most valuable information to merge together into the final image.

Fig. 13 shows that the information of high-density tissue in CT image and the features of higher moisture content tissue in MRI image are fused into the final image effectively. Specifically, the detailed edge and texture of the skull and brain cell were represented in the fused image; besides, the structural information of the eyes, ectocinerea, and alba were kept very well. Overall, the fused image generated by our proposed method is better than those of the control methods.

The brain medical images and the fused images generated by different methods are shown in Figs. 7–13. In general, the fused images from our proposed method are better than those of the other methods with regard to textures, details, and brightness. The experimental results show LPEWT fused more abundant details from the brain images than the other methods, and it extracted and fused the features of the brain

TABLE II

COMPUTATION TIME OF DIFFERENT IMAGE FUSION METHODS (CPU I5-4590@3.3 GHz, RAM 16 GB, MATLAB 2016A; "– –" REPRESENTS NULL)

GP[52]	DWT[52][53]	fsdP [52]	GFS [54]	CSR [55]	ASR [56]	GFF [57]	MSVD [58]	DTDWT [59]
0.0184	0.0273	0.0112	3.7029	45.8237	53.0404	0.0718	0.1495	0.1116
SWT[60][61]	CVT [62]	DTCWT-SR[63]	CVT-SR[63]	LRSDL [64]	PCLLE [65]	MSGIF [66]	DCHWT [67]	Proposed
0.2712	0.6756	1.1412	0.9851	– –	3.8704	0.0697	1.0911	2.4528

Fig. 12.　Experiments for S6. (a) CT. (b) MRI. (c) GP [52]. (d) DWT [52], [53]. (e) fsdP [52]. (f) GFS [54]. (g) CSR [55]. (h) ASR [56]. (i) GFF [57]. (j) MSVD [58]. (k) DTDWT [59]. (l) SWT [60], [61]. (m) CVT [62]. (n) DTCWT-SR [63]. (o) CVT-SR [63]. (p) LRSDL [64]. (q) PCLLE [65]. (r) MSGIF [66]. (s) DCHWT [67]. (t) Proposed.
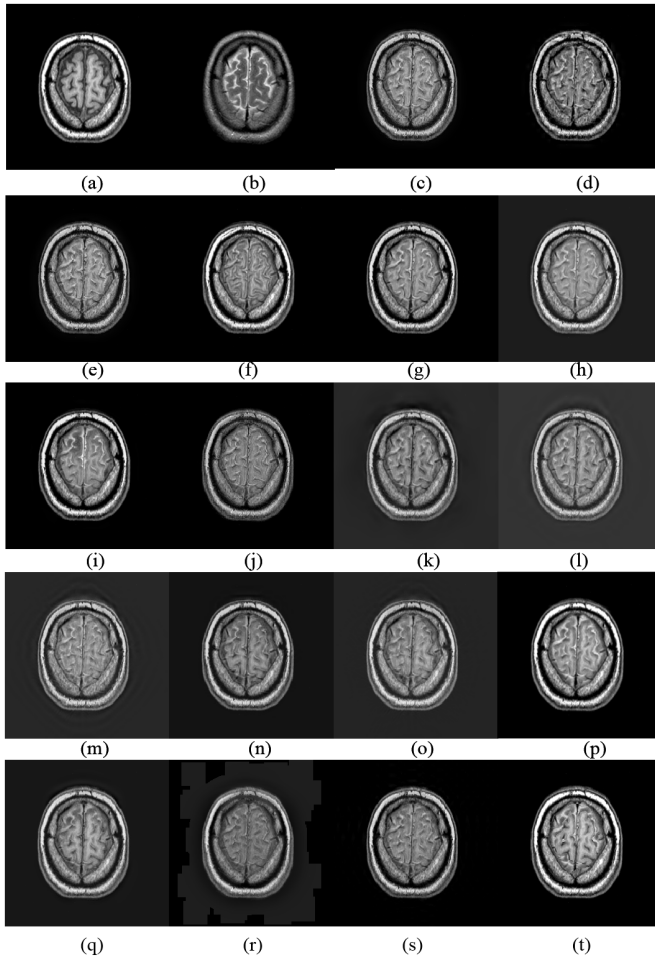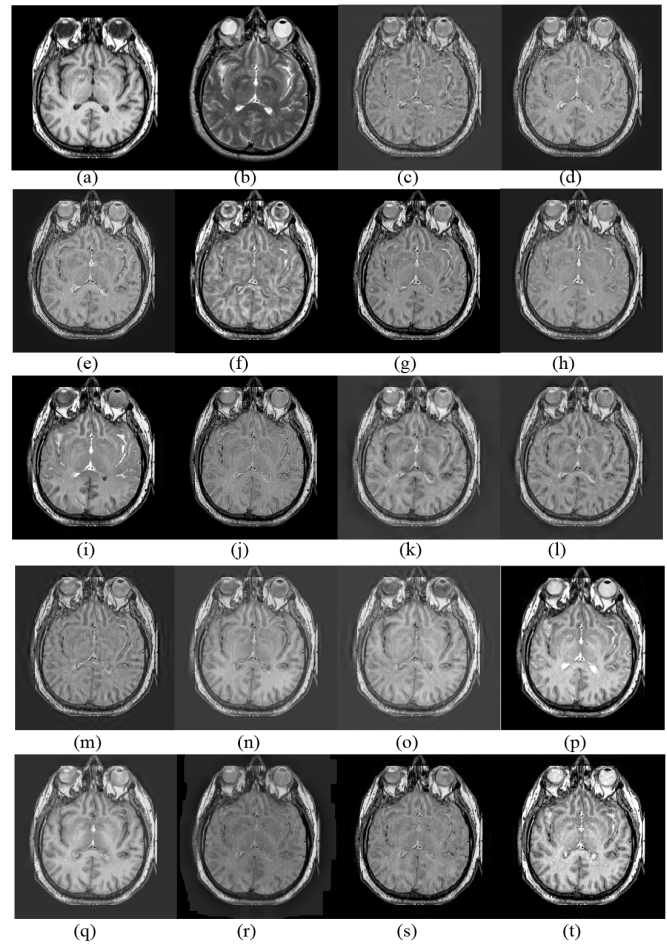

Fig. 13.　Experiments for S7. (a) CT. (b) MRI. (c) GP [52]. (d) DWT [52], [53]. (e) fsdP [52]. (f) GFS [54]. (g) CSR [55]. (h) ASR [56]. (i) GFF [57]. (j) MSVD [58]. (k) DTDWT [59]. (l) SWT [60], [61]. (m) CVT [62]. (n) DTCWT-SR [63]. (o) CVT-SR [63]. (p) LRSDL [64]. (q) PCLLE [65]. (r) MSGIF [66]. (s) DCHWT [67]. (t) Proposed.

images well. Overall, our proposed scheme is an effective and competitive medical image fusion method.

The averaged evaluation metrics for different image fusion methods are given in Table I and Fig. 14. Our scheme shows the highest Q^{abf} (as 0.6556), Q^{MI} (as 3.9071), Q^{te} (as 0.8664), and Q^{NCIE} (as 0.8111) values, demonstrating that the proposed method is effective to maintain key features of source images. Q^{abf} and Q^{MI} are the most important evaluation metrics in image fusion, and the values of the two metrics are apparently higher than those of other conventional methods, which shows that the proposed method can reserve more information of the medical images than other competitors. The value of L^{abf} of our proposed scheme is the lowest (as 0.2487), which means the fused images have minimal information loss. Although the Q^W and Q^{PC} values of our proposed scheme are not the best, they are close to the highest values (as 0.8439, 0.5766, respectively). In summary, the experiments reveal
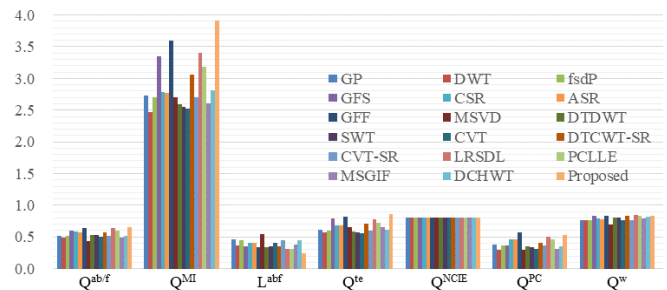

Fig. 14.　Histogram of averaged indexes.

that fused images generated by our proposed scheme are competitive compared with those of control methods, and the proposed medical image fusion method is effective.

We repeat ten times to calculate the average time as the computation time that is used to evaluate the computation

efficiency, and S6 is used as the example. The computation time of different image fusion methods is presented in Table II. The running time of conventional transform domain-based fusion methods, such as GP, DWT, and fsdP, are less than other complicated methods. Meanwhile, the computation of CSR and ASR is obviously complicated when compared with other fusion methods, but the running time of our proposed method is moderate. Nevertheless, our proposed method can achieve competitive results in visual effect and objective index.

V. CONCLUSION

In this study, we have proposed a new brain medical image fusion method using 2-D LPEWT, $L2$-norm-based features, and an MSFM method. 2-D LPEWT decomposes the medical image into a set of subimages, with the $L2$-norm-based features used to fuse the residue component, the MSFM method assists with fusing the IMFs, and inverse 2-D LPEWT reconstructs the fused image by considering the integrated filters. We have also designed a simple solution to the problem of differing numbers of IMFs between source images and made use of several image feature extraction methods for fusing the residue component and IMFs.

This article shows that 2-D LPEWT can be employed to handle the problem of image fusion. The experiments reveal that our proposed method effectively extracted and fused the features of the test brain medical images, and it was superior on several metrics and competitive on all when compared to other conventional methods. Our future work can be divided into two aspects. First, we plan to improve the performance of EWT-based image fusion method. Second, more fusion rules are supposed to explore according to the analysis of extracted image features.

ACKNOWLEDGMENT

REFERENCES

[1] D. V. Sorokin, I. Peterlik, M. Tektonidis, K. Rohr, and P. Matula, "Non-rigid contour-based registration of cell nuclei in 2-D live cell microscopy images using a dynamic elasticity model," *IEEE Trans. Med. Imag.*, vol. 37, no. 1, pp. 173–184, Jan. 2018.

[2] M. Yin, X. Liu, Y. Liu, and X. Chen, "Medical image fusion with parameter-adaptive pulse coupled neural network in nonsubsampled shearlet transform domain," *IEEE Trans. Instrum. Meas.*, vol. 68, no. 1, pp. 49–64, Jan. 2019.

[3] J. Du, W. Li, and B. Xiao, "Anatomical-functional image fusion by information of interest in local Laplacian filtering domain," *IEEE Trans. Image Process.*, vol. 26, no. 12, pp. 5855–5866, Dec. 2017.

[4] S. Liu, J. Jia, Y. D. Zhang, and Y. Yang, "Image reconstruction in electrical impedance tomography based on structure-aware sparse Bayesian learning," *IEEE Trans. Med. Imag.*, vol. 37, no. 9, pp. 2090–2102, Sep. 2018.

[5] A. P. James and B. V. Dasarathy, "Medical image fusion: A survey of the state of the art," *Inf. Fusion*, vol. 19, pp. 4–19, Sep. 2014.

[6] J. Du, W. Li, K. Lu, and B. Xiao, "An overview of multi-modal medical image fusion," *Neurocomputing*, vol. 215, pp. 3–20, Nov. 2016.

[7] S. Li, X. Kang, L. Fang, J. Hu, and H. Yin, "Pixel-level image fusion: A survey of the state of the art," *Inf. Fusion*, vol. 33, pp. 100–112, Jan. 2017.

[8] Z. Wang and Y. Ma, "Medical image fusion using m-PCNN," *Inf. Fusion*, vol. 9, no. 2, pp. 176–185, Apr. 2008.

[9] Q. Zhang, Y. Liu, R. S. Blum, J. Han, and D. Tao, "Sparse representation based multi-sensor image fusion for multi-focus and multi-modality images: A review," *Inf. Fusion*, vol. 40, pp. 57–75, Mar. 2018.

[10] Y. Liu, X. Chen, Z. Wang, Z. J. Wang, R. K. Ward, and X. Wang, "Deep learning for pixel-level image fusion: Recent advances and future prospects," *Inf. Fusion*, vol. 42, pp. 158–173, Jul. 2018.

[11] G. Qu, D. L. Zhang, and P. Yan, "Medical image fusion by independent component analysis," in *Proc. 5th Int. Conf. Electron. Meas. Instrum.*, 2001, pp. 887–893.

[12] H. Wang and H. Xing, "Multi-mode medical image fusion algorithm based on principal component analysis," in *Proc. Int. Symp. Comput. Netw. Multimedia Technol.*, 2009, pp. 1–4.

[13] H. Singh, J. Raj, G. Kaur, and T. Meitzler, "Image fusion using fuzzy logic and applications," in *Proc. IEEE Int. Conf. Fuzzy Syst.*, Feb. 2005, pp. 337–340.

[14] W. Zhao and H. Lu, "Medical image fusion and denoising with alternating sequential filter and adaptive fractional order total variation," *IEEE Trans. Instrum. Meas.*, vol. 66, no. 9, pp. 2283–2294, Sep. 2017.

[15] A. Sahu, V. Bhateja, A. Krishn, and H. Patel, "Medical image fusion with Laplacian pyramids," in *Proc. Int. Conf. Med. Imag., m-Health Emerg. Commun. Syst. (MedCom)*, Nov. 2014, pp. 448–453.

[16] T. Suriya and P. Rangarajan, "An improved fusion technique for medical images using discrete wavelet transform," *J. Med. Imag. Health Inform.*, vol. 6, no. 3, pp. 585–597, 2017.

[17] L. Yang, B. Guo, and W. Ni, "Multimodality medical image fusion based on multiscale geometric analysis of contourlet transform," *Neurocomputing*, vol. 72, nos. 1–3, pp. 203–211, Dec. 2008.

[18] L. Wang, B. Li, and L. Tian, "A novel multi-modal medical image fusion method based on shift-invariant shearlet transform," *J. Photographic Sci.*, vol. 61, no. 7, pp. 529–540, 2013.

[19] H. R. Shahdoosti and A. Mehrabi, "Multimodal image fusion using sparse representation classification in tetrolet domain," *Digit. Signal Process.*, vol. 79, pp. 9–22, Aug. 2018.

[20] A. Da Cunha, J. Zhou, and M. Do, "The nonsubsampled contourlet transform: Theory, design, and applications," *IEEE Trans. Image Process.*, vol. 15, no. 10, pp. 3089–3101, Oct. 2006.

[21] C. Zhao, Y. Guo, and Y. Wang, "A fast fusion scheme for infrared and visible light images in NSCT domain," *Infr. Phys. Technol.*, vol. 72, pp. 266–275, Sep. 2015.

[22] Y. Yang, Y. Que, S. Huang, and P. Lin, "Multimodal sensor medical image fusion based on type-2 fuzzy logic in NSCT domain," *IEEE Sensors J.*, vol. 16, no. 10, pp. 3735–3745, May 2016.

[23] X. Jin, G. Chen, J. Hou, Q. Jiang, D. Zhou, and S. Yao, "Multimodal sensor medical image fusion based on nonsubsampled shearlet transform and S-PCNNs in HSV space," *Signal Process.*, vol. 153, pp. 379–395, Dec. 2018.

[24] G. Bhatnagar, Q. M. J. Wu, and Z. Liu, "Directive contrast based multimodal medical image fusion in NSCT domain," *IEEE Trans. Multimedia*, vol. 15, no. 5, pp. 1014–1024, Aug. 2013.

[25] Y. Liu, X. Chen, J. Cheng, and H. Peng, "A medical image fusion method based on convolutional neural networks," in *Proc. 20th Int. Conf. Inf. Fusion (Fusion)*, Jul. 2017, pp. 1–7.

[26] J. Benjamin and T. Jayasree, "Improved medical image fusion based on cascaded PCA and shift invariant wavelet transforms," *Int. J. Comput. Assist. Radiol. Surg.*, vol. 13, no. 2, pp. 229–240, 2018.

[27] J. Sharma, K. Sharma, and V. Sahula, "Hybrid image fusion scheme using self-fractional Fourier functions and multivariate empirical mode decomposition," *Signal Process.*, vol. 100, pp. 146–159, Jul. 2014.

[28] B. Zhang *et al.*, "A medical image fusion method based on energy classification of BEMD components," *Optik-Int. J. Light Electron Opt.*, vol. 125, no. 1, pp. 146–153, 2014.

[29] H. R. Shahdoosti and Z. Tabatabaei, "MRI and PET/SPECT image fusion at feature level using ant colony based segmentation," *Biomed. Signal Process. Control*, vol. 47, pp. 63–74, Jan. 2019.

[30] A. Bhattacharya, D. Choudhury, and D. Dey, "Edge-enhanced bi-dimensional empirical mode decomposition-based emotion recognition using fusion of feature set," *Soft Comput.*, vol. 22, no. 3, pp. 889–903, Feb. 2018.

[31] S. Maheshwari, R. B. Pachori, and U. R. Acharya, "Automated diagnosis of glaucoma using empirical wavelet transform and correntropy features extracted from fundus images," *IEEE J. Biomed. Health Inform.*, vol. 21, no. 3, pp. 803–813, May 2017.

[32] T. N. Prabhakar and P. Geetha, "Two-dimensional empirical wavelet transform based supervised hyperspectral image classification," *ISPRS J. Photogram. Remote Sens.*, vol. 133, pp. 37–45, Nov. 2017.

[33] J. Zhang, H. Pan, S. Yang, and J. Cheng, "Adaptive parameterless empirical wavelet transform based time-frequency analysis method and its application to rotor rubbing fault diagnosis," *Signal Process.*, vol. 130, pp. 305–314, Jan. 2017.

[34] N. Huang *et al.*, "The empirical mode decomposition and the Hilbert spectrum for nonlinear and non-stationary time series analysis," *Proc. Math. Phys. Eng. Sci.*, vol. 454, no. 1971, pp. 903–995, 1998.

[35] T. Browne, V. Vittal, G. Heydt, and A. Messina, "A comparative assessment of two techniques for modal identification from power system measurements," *IEEE Trans. Power Syst.*, vol. 23, no. 3, pp. 1408–1415, Aug. 2008.

[36] T.-T. Tran *et al.*, "Empirical mode decomposition and monogenic signal-based approach for quantification of myocardial infarction from mr images," *IEEE J. Biomed. Health Inform.*, vol. 23, no. 2, pp. 731–743, Mar. 2019.

[37] J. Nunes, Y. Bouaoune, E. Delechelle, O. Niang, and P. Bunel, "Image analysis by bidimensional empirical mode decomposition," *Image Vis. Comput.*, vol. 21, no. 12, pp. 1019–1026, Nov. 2003.

[38] Y. Tian *et al.*, "Image fusion method based on EMD method," *Proc. SPIE*, vol. 5985, Jan. 2006, Art. no. 59854T.

[39] J. Gilles, "Empirical wavelet transform," *IEEE Trans. Signal Process.*, vol. 61, no. 16, pp. 3999–4010, Aug. 2013.

[40] L. Grafakos, "Classical Fourier analysis," *Springer*, vol. 249, no. 21, pp. 305–317, 2014.

[41] J. Gilles, G. Tran, and S. Osher, "2-D empirical transforms. Wavelets, ridgelets, and curvelets revisited," *SIAM J. Imag. Sci.*, vol. 7, no. 7, pp. 157–186, 2014.

[42] A. Averbuch, R. Coifman, D. Donoho, M. Elad, and M. Israeli, "Fast and accurate Polar Fourier transform," *Appl. Comput. Harmon. Anal.*, vol. 21, no. 2, pp. 145–167, Sep. 2006.

[43] A. Averbuch, R. R. Coifman, D. L. Donoho, M. Israeli, and Y. Shkolnisky, "A framework for discrete integral transformations I-the pseudopolar Fourier transform," *SIAM J. Sci. Comput.*, vol. 30, no. 2, pp. 764–784, Jan. 2008.

[44] J. Delon, A. Desolneux, J.-L. Lisani, and A. B. Petro, "A nonparametric approach for histogram segmentation," *IEEE Trans. Image Process.*, vol. 16, no. 1, pp. 253–261, Jan. 2007.

[45] Y. Xia and H. Leung, "A fast learning algorithm for blind data fusion using a novel L_2-norm estimation," *IEEE Sensors J.*, vol. 14, no. 3, pp. 666–672, Mar. 2014.

[46] Z. Lai, Y. Xu, J. Yang, J. Tang, and D. Zhang, "Sparse tensor discriminant analysis," *IEEE Trans. Image Process.*, vol. 22, no. 10, pp. 3904–3915, Oct. 2013.

[47] Z. Lai, Y. Xu, Z. Jin, and D. Zhang, "Human gait recognition via sparse discriminant projection learning," *IEEE Trans. Circuits Syst. Video Technol.*, vol. 24, no. 10, pp. 1651–1662, Oct. 2014.

[48] Q. Wang, Q. Gao, X. Gao, and F. Nie, "$l_{2,p}$-norm based PCA for Image Recognition," *IEEE Trans. Image Process.*, vol. 27, no. 3, pp. 1336–1346, Mar. 2018.

[49] S. Yu *et al.*, "L2-norm multiple kernel learning and its application to biomedical data fusion," *BMC Bioinf.*, vol. 11, no. 1, pp. 309–332 Dec. 2010.

[50] C.-I. Chen, "Fusion of PET and MR brain images based on IHS and log–Gabor transforms," *IEEE Sensors J.*, vol. 17, no. 21, pp. 6995–7010, Nov. 2017.

[51] P. Burt and R. Kolczynski, "Enhanced image capture through fusion," in *Proc. 4th Int. Conf. Comput. Vis.*, May 1993, pp. 173–182.

[52] R. Oliver. (Sep. 30, 1999). *Pixel-Level Image Fusion and the Image Fusion Toolbox*. [Online]. Available: http://www.metapix.de/fusion.htm

[53] N. Li, B. Manjunath, and S. Mitra, "Multi-sensor image fusion using the wavelet transform," in *Proc. 1st Int. Conf. Image Process.*, Nov. 1994 pp. 51–55.

[54] D. P. Bavirisetti, V. Kollu, X. Gang, and R. Dhuli, "Fusion of MRI and CT images using guided image filter and image statistics," *Int. J. Imag. Syst. Technol.*, vol. 27, no. 3, pp. 227–237, Sep. 2017.

[55] Y. Liu, X. Chen, R. K. Ward, and Z. J. Wang, "Image fusion with convolutional sparse representation," *IEEE Signal Process. Lett.*, vol. 23, no. 12, pp. 1882–1886, Dec. 2016.

[56] Y. Liu and Z. Wang, "Simultaneous image fusion and denoising with adaptive sparse representation," *IET Image Process.*, vol. 9, no. 5, pp. 347–357, May 2015.

[57] S. Li, X. Kang, and J. Hu, "Image fusion with guided filtering," *IEEE Trans. Image Process.*, vol. 22, no. 7, pp. 2864–2875, Jul. 2013.

[58] V. Naidu, "Image fusion technique using multi-resolution singular value decomposition," *Defence Sci. J.*, vol. 61, no. 5, p. 479, Jul. 2017.

[59] D. Renza, E. Martinez, and A. Arquero, "Quality assessment by region in spot images fused by means dual-tree complex wavelet transform," *Adv. Space Res.*, vol. 48, no. 8, pp. 1377–1391, Oct. 2011.

[60] G. P. Nason and B. W. Silverman, "The stationary wavelet transform and some statistical applications," *Wavelets and Statistics*. New York, NY, USA: Springer, 1995, pp. 281–299.

[61] K. Liu, L. Guo, and L. Hui, "Image fusion algorithm using stationary wavelet transform," *Comput. Eng. Appl.*, vol. 43, no. 12, pp. 59–61, 2007.

[62] J.-L. Starck, E. Candes, and D. Donoho, "The curvelet transform for image denoising," *IEEE Trans. Image Process.*, vol. 11, no. 6, pp. 670–684, Jun. 2002.

[63] Y. Liu, S. Liu, and Z. Wang, "A general framework for image fusion based on multi-scale transform and sparse representation," *Inf. Fusion*, vol. 24, pp. 147–164, Jul. 2015.

[64] H. Li, X. He, D. Tao, Y. Tang, and R. Wang, "Joint medical image fusion, denoising and enhancement via discriminative low-rank sparse dictionaries learning," *Pattern Recognit.*, vol. 79, pp. 130–146, Jul. 2018.

[65] Z. Zhu, M. Zheng, and G. Qi, "A phase congruency and local Laplacian energy based multi-modality medical image fusion method in NSCT domain," *IEEE Access*, vol. 7, pp. 20811–20824, 2019.

[66] D. Bavirisetti1, G Xiao, and J Zhao, "Multi-scale guided image and video fusion: A fast and efficient approach," *Circuits, Syst., Signal Process.*, to be published.

[67] B. Kumar, "Multifocus and multispectral image fusion based on pixel significance using discrete cosine harmonic wavelet transform," *Signal, Image Video Process.*, vol. 7, no. 6, pp. 1125–1143, 2013.

[68] C. Xydeas and V. Petrovic, "Objective image fusion performance measure," *Electron. Lett.*, vol. 36, no. 4, pp. 308–309, 2000.

[69] G. Qu, D. Zhang, and P. Yan, "Information measure for performance of image fusion," *Electron. Lett.*, vol. 38, no. 7, p. 313, 2002.

[70] G. Piella and H. Heijmans, "A new quality metric for image fusion," in *Proc. Int. Conf. Image Process.*, Sep. 2003, pp. III:173–III:176.

[71] J. Zhao, R. Laganiere, and Z. Liu, "Performance assessment of combinative pixel-level image fusion based on an absolute feature measurement," *Int. J. Innov. Comput. Inf. Control*, vol. 3, no. 6, pp. 1433–1447, 2007.

[72] Q. Wang, Y. Shen, and J. Jin, "Performance evaluation of image fusion techniques," *Image Fusion, Algorithms Appl.*, vol. 19, pp. 469–492, Jun. 2008.

[73] N. Cvejic, C. Canagarajah, and D. Bull, "Image fusion metric based on mutual information and Tsallis entropy," *Electron. Lett.*, vol. 42, no. 11, p. 626, 2006.
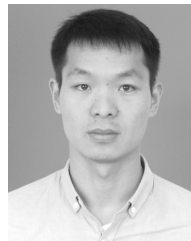
Xin Jin received the B.S. degree in electronics and information engineering from Henan Normal University, Xinxiang, China, in 2013, and the Ph.D. degree in communication and information systems from Yunnan University, Kunming, China, in 2018.

He holds a post-doctoral position at the School of Software, Yunnan University. His current research interests include pulse coupled neural networks theory and its applications, image processing, optimization algorithm, and bioinformatics.

Qian Jiang received the B.S. degree in thermal energy and power engineering and the M.S. degree in power engineering and engineering thermophysics from Central South University (CSU), Changsha, China, in 2012 and 2015, respectively. She is currently pursuing the Ph.D. degree with the School of Information, Yunnan University, Kunming, China.

Her research interests include machine learning, bioinformatics, and image processing.

Xing Chu received the B.E. degree from the Kunming University of Science and Technology, Kunming, China, in 2011, the M.E. degree from Hunan University, Changsha, China, in 2014, and the Ph.D. degree in control theory and engineering from the École Centrale de Lille, Villeneuve-d'Ascq, France, in 2017.

He is currently an Associate Professor with the School of Software, Yunnan University, Kunming. His research interests lie in distributed cooperative control of multiagent/robot systems and intelligent automobile.

Xun Lang was born in 1994. He received the B.S. and Ph.D. degrees in automation from Zhejiang University, Hangzhou, China, in 2014 and 2019, respectively.

He holds a post-doctoral position at the School of Information, Yunnan University, Kunming, China. His current research interests include, but are not limited to, process control performance monitoring, signal processing, and time–frequency analysis.

Keqin Li (Fellow, IEEE) is currently a SUNY Distinguished Professor of computer science with the State University of New York, New Paltz, NY, USA. He has published over 690 journal articles, book chapters, and refereed conference papers. His current research interests include cloud computing, fog computing and mobile edge computing, energy-efficient computing and communication, embedded systems and cyber-physical systems, heterogeneous computing systems, big data computing, high-performance computing, CPU–GPU hybrid and cooperative computing, computer architectures and systems, computer networking, machine learning, and intelligent and soft computing.

Prof. Li has received several best paper awards. He currently serves or has served on the Editorial Board of the IEEE Transactions on Parallel and Distributed Systems, the IEEE Transactions on Computers, the IEEE Transactions on Cloud Computing, the IEEE Transactions on Services Computing, and the IEEE Transactions on Sustainable Computing.

Shaowen Yao received the B.S. and M.S. degrees in telecommunication engineering from Yunnan University, Kunming, China, in 1988 and 1991, respectively, and the Ph.D. degree in computer application technology from the University of Electronic Science and Technology of China (UESTC), Chengdu, China, in 2002.

He is currently a Professor with the School of Software, Yunnan University. His current research interests include neural network theory and applications, cloud computing, and big data computing.

Wei Zhou (Member, IEEE) received the Ph.D. degree from the University of Chinese Academy of Sciences, Beijing, China.

He is currently a Professor and a Full Professor with the School of Software, Yunnan University, Kunming, China. His current research interests include distributed data intensive computing and bioinformatics.